PNAS
www.pnas.org

Supplementary Information for

Dissecting Fat-Tailed Fluctuations in the Cytoskeleton with Active Micropost Arrays

Yu Shi, Christopher L. Porter, John C. Crocker, Daniel H. Reich

Corresponding Authors: J. C. Crocker and D. H. Reich
Email: jcrocker@seas.upenn.edu, reich@jhu.edu

This PDF file includes:

Supplementary text
Table S1
Figs. S1 to S12
References for SI reference citations

www.pnas.org/cgi/doi/10.1073/pnas.1900963116

Supplementary Information Text

Methods

Magnetic micropost array fabrication. Active micropost array detectors (AMPADs) were made of polydimethylsiloxane (PDMS) via replica molding (1) on standard glass coverslips. PDMS negative molds were produced from silicon masters made by photolithography and deep reactive ion etching (2). The AMPAD devices had microposts 1.8 μm in diameter and 6.4 μm in height in hexagonal arrays with near-neighbor spacing of 4 μm. For small deflections in response to lateral forces applied at their tips, these microposts had an effective spring constant k =15.7 nN/μm. The silicon masters have < 1% variation in the micropost diameter d (2), leading to an estimate of ≤ 4% variation in k, as $k \propto d^4$ from elementary beam bending theory.

Magnetic nickel nanowires were fabricated by electrodeposition in nanoporous templates (3). The nanowires had length 5 μm, diameter 350 nm, with 10% uncertainty in each dimension and average low-field magnetic moments of $\mu = 0.15$ pA·m^2, aligned along their long axes (4, 5). To embed nanowires in a subset of the microposts for magnetic actuation experiments, nanowires in ethanol suspensions (10^6 /ml) were placed on negative molds prior to casting AMPAD arrays, and the nanowires were drawn down into the micropillar molds by placing a rare-earth magnet underneath the molds and then allowing the ethanol to evaporate (6, 7). Approximately 1% of the microposts contained a magnetic nanowire. The maximum misalignment of a nanowire in a micropost allowed by the posts' geometry is ±20°, but to minimize this, the PDMS was cured with a magnetic field applied.

To promote cell adhesion at the tops of the microposts and to ensure that the posts were coupled to the cellular actomyosin network, we functionalized the microposts' tops with fibronectin through microcontact printing (1, 8). The posts' sides and the remaining surfaces of the arrays were blocked from cell adhesion with by coating with 0.2% W/V Pluronics F-127 solutions (ThermoFisher Scientific).

Cell culture. NIH 3T3 fibroblasts (ATCC) were cultured in high glucose Dulbecco's modified Eagle medium (DMEM) (Corning Cellgro) containing 10% bovine serum (ThermoFisher Scientific), 100 units/mL penicillin, and 100 mg/mL streptomycin (Life Technologies) at 37℃ in 5% CO_2. For measurements, the cells were suspended via trypsin/EDTA and then seeded onto

AMPAD devices in 35 mm culture dishes at a concentration of 1000 cells/ml. The cells were incubated overnight in the above culture conditions to enable them to adhere and spread on the microposts. During microscopy measurements, the cells were maintained at 37℃ with a microscope enclosure incubator (InVivo Scientific), together with a stage-mounted heating plate (TC-500, 20/20 Technology). Passive measurements of cell dynamics were carried out at 5% CO_2 in the incubator's environmental sub-chamber. Magnetic actuation measurements were done in CO_2-independent medium (Life Technologies) containing 4% L-glutamine, 10% bovine serum (ThermoFisher Scientific), 100 units/mL penicillin, and 100 mg/mL streptomycin (Life Technologies), as the environmental sub-chamber could not accommodate the magnetic tweezers.

Measurements of micropost dynamics. Measurements of the microposts' motion were made on a Nikon TE-2000E inverted microscope, using a 40x, NA = 0.6, extra-long working distance air objective (Nikon Plan Fluor). Illumination was provided via a stock 100 W halogen illuminator and a long-working distance condenser with NA = 0.52. Bright field movies were recorded at sampling frequencies f_S up to 100 frames/s at 4.5 ms exposure time with a Prosilica GX-1050 CCD camera (Allied Vision Technologies) using the StreamPix software suite (Norpix). For optimum spatial resolution of the microposts' positions, we maximized the microscope's condenser aperture, and used the maximum illuminator intensity achievable without saturating the camera. The camera's digital gain was turned off to minimize camera noise. To enable these high illumination intensities without affecting cell viability, ultraviolet (Edmund Optics #64-667) and infrared (Edmund Optics #47-303) filters were used to restrict the incident light to the wavelength range 425 nm < λ < 700 nm. Cells were found to remain proliferative following 18 h exposure to our experimental observation conditions.

Magnetic tweezers and local cellular rheology measurements. A dual magnetic tweezer system (8) was used to actuate the magnetic microposts. Two solenoids were each mounted on 3-axis micromanipulator stages. The solenoids each had iron cores with finely sharpened pole tips that when positioned 0.5 mm apart and 0.8 mm above the microposts arrays provided an approximately spatially uniform magnetic field that could be localized on an individual cell. We used a custom-built sample dish with an indented lid to enable the tweezer tips to be brought within 1 mm of the cells without touching the culture media (Supplementary Fig. S10). The

culture media filled the space between the sample and a glass window in the lid to eliminate any image distortion associated with an air-liquid interface in the optical path. The solenoids were connected in series, and were driven by a Kepco BOP 50-2M power supply controlled by digitally synthesized waveforms from a National Instruments PCIe-6231 DAQ card controlled by the StreamPix software. Sinusoidal magnetic fields of amplitude 10 mT were used to produce magnetic torques with amplitudes 1.5 nN·μm on the nanowires that led to effective forces F_{mag} with amplitude 250 pN applied to the portion of the cell adherent to the magnetic microposts (6, 7). Videos were recorded at f_S = 100 frames/s and Hall sensors attached at the back of the magnetic tweezer's iron cores monitored the magnetic field, which was recorded synchronously with each video frame via the DAQ card. The frequency f of the magnetic field was varied in the range 0.1 Hz ≤ f ≤ 135 Hz. A second sinusoidal field at a fixed reference frequency f_R = 7 Hz was applied simultaneously with that at f to enable a ratiometric measurement of the response to account for temporal variations in the cell-post coupling (See below.) (9). Measurement times were 180 s for f ≤ 1 Hz, 60 s for 1 Hz < f ≤ 10 Hz, and 30 s for f > 10 Hz. The cells were subsequently removed from the AMPAD arrays with tripsin/EDTA, and the measurements were repeated to obtain the background frequency-dependent viscoelasticity of the individual magnetic microposts alone, to account for any post-to-post variations.

Determination of microposts' motion. The microposts' positions vs. time were determined using an implementation of a centroid-based particle tracking algorithm (10) written in Igor Pro (Wavemetrics). To account for frame-to-frame drift, the average displacement in each frame relative to the initial frame of all microposts not in contact with cells (background posts) was subtracted from all individual micropost trajectories. Due to very slight non-linearities in the mapping from physical location to centroided position, the residual RMS amplitude in background posts' motion after this process was about 2-3 nm over the course of 30 minutes, which is insignificant compared with the typical motion from cells that we observed. The undeflected positions of posts in contact with cells were determined by interpolation based on the positions of the background posts in the corresponding rows and columns of the AMPAD array (7).

Analysis of magnetically actuated cellular rheology measurements. The amplitudes and phases of the magnetic microposts' response at the frequencies f and f_R were found via digital

lock-in analysis (11) of the microposts' positions **r**(t) determined from the image sequences. The results were corrected for frequency dependent reductions in amplitude due to the finite exposure time, and phase shifts arising from both the exposure time and the fixed lag time between the camera exposure window and the sampling of the magnetic field by the DAQ card. Data at frequencies above the Nyquist frequency $f_{Ny} = f_S/2 = 50$ Hz were measured via aliasing, *i.e.* at apparent frequencies $f' = 100$ Hz $- f$ for 50 Hz $< f <$ 100 Hz, and at $f' = f - 100$ Hz for $f >$ 100 Hz. This approach yielded AC amplitude resolution $\delta r < 0.2$ nm. The component of micropost motion perpendicular to the magnetic field $y(\omega)$ was on average 7 ± 5% of the motion $x(\omega)$ parallel to the field for magnetic microposts not attached to the cells. This is attributable to a combination of the ~1% variation of the field direction over the field of view of our microscope and small misalignment of the field axis due to the positioning of the magnetic tweezer tips. These transverse motions are linear in the field for all posts, and hence do not hinder our quantification of the cells' power-law rheology.

To assess the variation in the amplitudes at each frequency, we broke up each measurement interval into 2-s sub-intervals (Fig. S2A) or 10-s sub-intervals (all other data), and carried out the digital lock-in analysis on each sub-interval. The amplitude variation on the full interval was estimated as the standard error computed from the set of sub-intervals. These errors were used to quantify the uncertainties in the determination of the post and cell stiffnesses $k(\omega)$ and $k_{cell}(\omega)$ as described below.

To account for the observed temporal fluctuations in $x(\omega)$ (Supplementary Fig. S2), the ratio

$$x(\omega) = \frac{x_s(\omega)}{x_R(\omega_R)} \cdot \overline{x}_R(\omega_R)$$

was computed (9), where $x_s(\omega)$ was the response at the variable frequency f and $x_R(\omega_R)$ was the response at the reference frequency f_R over the same measurement interval. The ratio of those two signals was multiplied by $\overline{x}_R(\omega_R)$, the average of $x_R(\omega_R)$ over all the measurement intervals, to keep the average of $x(\omega)$ unchanged. This ratiometric approach yielded greatly reduced fluctuations in $x(\omega)$ compared with those in $x_s(\omega)$ (Supplementary Fig. S2*B*). The magnetic force $F(\omega)$ was determined from the measured magnetic field $B(\omega)$, using the

nanowires' magnetic moment and the nanowires' and microposts' dimensions (7). The equivalent stiffness was then calculated as $k(\omega)= F(\omega)/x(\omega)$. The posts' stiffness $k_{post}(\omega)$ was determined from the data obtained following removal of the cells by trypsinization, and the resulting cell stiffness computed as $k_{cell}(\omega) = k(\omega) - k_{post}(\omega)$ (Supplementary Fig. S2*C*-*E*). Below f = 50 Hz, $k_{cell}(\omega)$ was dominated by the storage modulus, and so we made power law fits to $|k_{cell}(\omega)|$ up to 20 Hz. The resulting exponents were not sensitive to varying this cutoff in the range 5 – 20 Hz. There was a ~30% systematic uncertainty in the measurement of the magnitude of the stiffness due to variations in the magnetic torque applied by the nanowires. This is dominated by the ~25% uncertainty in the nanowires' magnetic moment due to polydispersity in their volume (see above), and there is an additional variation of up to ~6% in the magnetic torque due to possible misalignment of each nanowire from vertical (up to 20°). However, we note that the measurements of the power-law dependence of $k_{cell}(\omega)$ were insensitive to this effect.

Analysis of cellular mechanical fluctuation measurements. We characterized the microposts' deflection traces using the mean square displacement (MSD) $\langle \Delta r^2(\tau) \rangle = \langle (\mathbf{r}(t+\tau) - \mathbf{r}(t))^2 \rangle$. We only computed MSDs for τ up to 1/5 of the video length to ensure sufficient averaging for each data point. Video lengths of 1,800 s (at 10 frames/s) were used to ensure that the MSDs were recorded accurately for τ up to 360 s. To extract the MSD exponent α for each post, we obtained the post's noise floor by fitting the MSD trace for $\tau \leq 1$ s to the form

$$MSD = C + D\tau^q \ ,$$

and subtracted the constant C from the MSD traces to obtain the "subtracted MSD," MSD_{Sub}. We then calculated the logarithmic time derivative $\frac{d\log(MSD_{Sub})}{d\log\tau}$, and averaged its value between 5 s $\leq \tau \leq$ 10 s to obtain α and its uncertainty. This procedure is illustrated in Supplementary Fig. S11.

To identify posts not engaged by cells, we analyzed the MSDs of background posts far from cells and found that MSD exponents $\alpha < 0.5$ provided a robust criterion. As measurement times up to 1,800 s were used, cell motility could lead to microposts being engaged with a cell over only part of the measurement window. To identify such posts, we calculated the MSD of each post separately for the first third and the last third of each video, and determined the

corresponding MSD exponents α_1 and α_3 for those intervals in the range 5 s ≤ τ ≤ 10 s, using the approach described above. Only microposts that were engaged with a cell for both of the above intervals (i.e., had both α_1 and $\alpha_3 > 0.5$) were included in subsequent analysis. Examples of micropost traces corresponding to these various conditions are shown in Supplementary Fig. S4.

To separate the cell-coupled microposts into subpopulations associated with different components of the cytoskeleton, we used the average traction force on each post, measured over the full measurement window, and calculated based on the spring constant of the microposts, k = 15.7 nN/μm. We identified as stress fiber posts those with average traction forces larger than 5 nN, and as cortical posts those with maximum traction force less than 2 nN. Examples of time traces for microposts that satisfied these two conditions, as well as for one rejected by this method are shown in Supplementary Fig. S4*D*-*F*.

Angular probability distribution function. To parametrize the widths of the probability distributions of the orientations of the anisotropy index ellipses for the cortical and stress fiber microposts, we fit the data in Fig. 4*D* and Supplementary Fig. S7*B* to a version of the von Mises circular normal distribution function with period π plus a constant offset,

$$P(\theta) = A\frac{e^{\kappa \cos 2(\theta-\theta_0)}}{\pi I_0(\kappa)} + B.$$

Here $I_0(\kappa)$ is the modified Bessel function of order 0, and the full width of the peak in $P(\theta)$ is $2\sigma = 1/\sqrt{\kappa}$.

Non-Gaussian parameter for displacement distributions. To assess the intermittency of individual microposts' deflections (Fig. 5), the posts' trajectories were each cut into six 300 s segments from each 1,800 s movie. MSDs were calculated for each trajectory, and $L_{MSD} = [MSD(\tau)]^{1/2}$ at τ = 20 s and 100 s was also calculated. To quantify the intermittency of individual posts, the non-Gaussian parameter

$$\alpha_2 = \frac{\langle x^4 \rangle}{3\langle x^2 \rangle^2} - 1$$

was then calculated for each post, based on segmenting each 1,800 s trajectory into 20 s and 100 s intervals. Here, $\langle x^2 \rangle$ and $\langle x^4 \rangle$ are the 2nd and 4th moments of the set of 90 displacements for each of the 20 s intervals and the set of 18 displacements for the 100 s intervals contained in each post's 1,800 s trajectory, respectively. For comparison, the same analysis was also applied to simulated random walks of the same length.

Pharmacological treatments. For myosin inhibition studies, we first measured cells' baseline mechanical fluctuations by imaging microposts for 90 s at 100 frames/s and then switched to media with either 60 nM blebbistatin or 50 nM Y27632. After 30 minutes incubation, the cells' fluctuations were re-measured for an additional 90 s. The cells were then fixed and stained for f-actin and nuclei for morphological comparison to untreated controls via immunofluorescence microscopy. For ATP depletion studies, mechanical fluctuations were measured for 90 s as above, before and after 30 min. incubation in DMEM with 50 mM 2-D-deoxyglucose and 0.05% NaN3 (Alfa Aesar, Ward Hill, MA) (9, 12).

Immunofluorescence microscopy. For immunofluorescence microscopy, cells were fixed in Formalin solution (Sigma-Aldrich), permeablized in 0.1% Triton-X and stained for f-actin with TRITC-phalloidin (Invitrogen) and for nuclei with Hoechst (Life Technologies). Images were taken with a 40x water immersion objective on a Leica SP8 confocal microscope. Two images of a single focal plane were averaged to reduce background noise.

Coincidence detection of large cortical avalanche-like events. To identify large anti-correlated motions within near-neighbor micropost pairs, we broke the 1,800 s observation window of each cell into 90 s intervals, and first calculated the Pearson correlation coefficient for all near-neighbor, cortically associated micropost pairs. For each pair, the posts' deflections $\vec{r}_1(t)$ and $\vec{r}_2(t)$, measured relative to the posts' undeflected positions $\vec{R}_{01}$ and $\vec{R}_{02}$, respectively, were projected onto the line connecting the undeflected positions, $\vec{R}_{12} = \vec{R}_{01} - \vec{R}_{02}$. The Pearson coefficient of the parallel components of the posts' motion, $u_1 = |\vec{r}_1| \cos\theta_1$ and $u_2 = |\vec{r}_2| \cos\theta_2$, was calculated over the N = 900 video frames in each 90 s interval as

$$P = \frac{\sum_{i=1}^{N} (u_{1,i} - \bar{u}_1)(u_{2,i} - \bar{u}_2)}{\sqrt{\left(\sum_{i=1}^{N} (u_{1,i} - \bar{u}_1)^2 \right) \left(\sum_{j=1}^{N} (u_{2,j} - \bar{u}_2)^2 \right)}},$$

where $\bar{u} = \frac{1}{N}\sum_{i=1}^{N} u_i$ is the average over the interval. θ_1 is the angle between $\vec{r}_1(t)$ and $\vec{R}_{12}$, and θ_2 is the angle between $\vec{r}_2(t)$ and $\vec{R}_{12}$. Pairs with $P < -0.7$ on an interval were then further selected based on their motions parallel and perpendicular to $\vec{R}_{12}$ within that interval. Pairs with either perpendicular displacement $\Delta v = v_{\max} - v_{\min} > 30$ nm for either post, where $v_{\max}$ and $v_{\min}$ are the maximum and minimum values over the 90 s interval of the component of the post deflection $v = |\vec{r}|\sin\theta$ perpendicular to $\vec{R}_{12}$, or with parallel displacement $\Delta u = u_{\max} - u_{\min} < 20$ nm for either post were discarded. Application of these criteria to 14 cells (from 3 independent trials) and to 25 additional cells with single 90 s data ensembles (from 5 independent trials) with a total of 4848 near-neighbor low-traction force post pairs yielded a dataset of 359 micropost pairs with highly anti-correlated motion directed largely along their line of centers.

We then identified from within this dataset events containing synchronized steps in the deflection traces of both posts within a pair that were opposite in direction (i.e., anticorrelated). The parallel components of the posts' trajectories $u(t)$ were smoothed via boxcar averaging over a 10 s range, and then the 1st derivative du_s/dt of the smoothed traces $u_s(t)$ was computed. Peaks in the 1st derivative traces with absolute value $|du_s/dt| > 4$ nm/s were identified using the Igor Pro software's built-in peak finder, and their positions were then refined by fitting the du_s/dt data with a 2nd order polynomial over an 8 s interval centered on the initially identified peak. This yielded measurements of the peak positions that were accurate to 0.1 s. This accuracy was determined from uncertainties in the parameters of the polynomial fits, which were estimated from the range for each parameter where χ^2 increased from its minimum value by the factor $(1 + 1/N_{\text{free}})$, where $N_{\text{free}} = N_{\text{data-points}} - N_{\text{model-parameters}}$ is the number of free parameters (13). Pairs with synchronized steps were then identified as those where peaks from each post were within 5 s of each other. We also required that the steps lasted for at least 5 data points (0.5 seconds) to prevent inclusion of errors in tracking the microposts' positions. This restriction, combined with the threshold on velocity for step detection described above, enabled us to pick out step events with large amplitudes while excluding effects due to low frequency noise. We note that this introduced a lower bound for possible step detection (0.5 s duration), whereas the threshold on

velocity may have excluded some long-duration events. Therefore, our observed anti-correlated motions likely do not represent the overall time scale distribution of avalanche-like events that may exist in cells. We found 68 synchronized step events via this method. As a control, application of this full analysis procedure to a sample of 4848 randomly selected non-near neighbor pairs yielded only 2 events that passed all the criteria.

To quantify the steps in the posts' deflections, we fit the unsmoothed trajectories $u(t)$ centered over a ±20 s range about the peak positions in du/dt with error functions $f(t) = A + h \cdot erf(\frac{t - t_0}{\Delta t})$, where $erf(x) = \int_{-x}^{x} e^{-z^2}\, dz$, to obtain each step's characteristic duration Δt and height h. Uncertainties in the fit parameters were estimated as described in the previous paragraph.

To obtain a measure of the average shape of a step, we selected events with height ratios in the range $0.7 < h_2/h_1 < 1.4$ for the two posts in the pair, and also with h_2 and $h_1 > 6$ nm. From the population of 68 events, this yielded 19 expanding and 12 contracting events, which were then used in the analysis described in Figs. 6*E* and *F*.

To assess the possibility of dipolar deformations, we searched for near neighbor micropost pairs with highly correlated parallel motion ($P > 0.7$, $\Delta u > 20$ nm, $\Delta v < 30$ nm). This yielded 437 candidate pairs, but none showed synchronized correlated steps. We also searched for highly anti-correlated tangential motion within pairs ($P < -0.7$, $\Delta u < 30$ nm, $\Delta v > 20$ nm). This yielded 17 candidate pairs, of which none showed synchronized anti-correlated steps.

Statistics

The data for pharmacological treatments (Fig. 2*G* and Supplementary Fig. S6*T-V*) were analyzed via unpaired t-tests. Examples of the distributions of the MSD exponents α_c and α_{sf} for both the cortically associated and stress fiber associated posts are shown for four cells in Fig. 3*C*, and the data for our full set of 14 cells are summarized in Supplementary Table S1. As illustrated in Fig. 3, there are differences in cortical and stress fiber associated posts within each cell, but there is also variability between cells in the averages of the exponent distributions. There is also significant spread in exponent values within each cell. As a measure of this we note that the

average standard deviations are $\delta\alpha_c = 0.20 \pm 0.02$ (mean ± SD, $N_{cells} = 14$) for the cortical posts, and $\delta\alpha_{sf} = 0.17 \pm 0.04$ (mean ± SD, $N_{cells} = 13$) for the stress fiber-associated posts.

We found that the cell-to-cell variations in α_c for the cortical posts are significant via a one-way ANOVA test with $p < 0.001$ over the full data set. For the stress-fiber associated posts we find variations in α_{sf} are also significant via one-way ANOVA with $p = 0.045$ for a sample consisting of all nine cells with >2 such posts.

The exponent α_{sf} is greater than α_c across the population as confirmed by a paired t-test based on the averaged exponent for each individual cell, excluding the cell (Cell 8 in Table S1) with no stress fiber posts, $p < 0.001$ ($N = 13$).

On the basis of these features of the data we chose to report the exponent values for the posts associated with the two types of subcellular structures (cortex and stress fibers) as the average of the cell-averages, rather than averaging all the individual posts directly. This approach yields $\bar{\alpha}_c = 1.17 \pm 0.02$ (SE, $N_{cells} = 14$) and $\bar{\alpha}_{sf} = 1.47 \pm 0.02$ (SE, $N_{cells} = 13$), respectively.

Assessment of impact of fluctuations in cellular optical density.

As we measured the microposts' positions via white light imaging through the cells, there could be some spurious contributions to the microposts' apparent fluctuating motion and MSDs due to fluctuations in the local optical density of the cell over each micropost, arising from internal cellular rearrangements, such as organelle trafficking. To isolate and assess the impact of this effect we used posts which appeared to be transiently disconnected from the cytoskeleton, by virtue of their having very small traction force in both the x and y direction, as in those intervals any confounding contributions to fluctuations in their apparent positions due to optical density effects should be most apparent. Specifically, we searched the set of microposts that the discrimination system described above (Methods: Analysis of cellular mechanical fluctuation measurements.) identified as engaged with and hence under the cell for the full 1,800 s window for 300 s time segments during which a micropost's deflections from its resting position, Δx and Δy, were both always < 15 nm (i.e., maximum traction force < 0.24 nN). The high-traction force microposts were excluded from this analysis. We found 159 such time segments over our set of 14 cells (~1% of the full micropost data set) (Supplementary Fig. S12). Based upon their low

traction force, we identified these posts as not mechanically coupled to the cytoskeleton during that 300 s interval. This identification was confirmed by repeating the analysis but substituting a fictitious resting position for the micropost displaced a small distance from the true location, and counting how many posts/intervals still satisfied the Δx, $\Delta y < 15$ nm condition. When the resting location was displaced by just 50 nm, the number dropped from 159 to ~10, which we took to be the "accidental rate" to pass the above screen.

The MSDs for a representative sample comprising 53 of these time segments are shown in Supplementary Fig. S12*A*, together with the average MSD computed for all 159 segments. The fluctuations reflected in these MSDs provide a measure of the optical noise added to the position determination of the posts (centroiding) due to the cellular rearrangements over the microposts. While these time segments do show MSDs that are above the noise floor as measured by background posts far from a cell, as expected for optical noise, the average MSD for these segments is below 20 nm^2 at $\tau = 100$ s and the largest one is only ~40 nm^2. These deflections are more than a factor of 10 smaller than for typical low-traction force posts for lag times $\tau > 10$ s. Thus, such optical density fluctuation effects appear to be at most a small contribution to the microposts' MSDs.

We also considered effects that could arise if the optical centroiding noise were highly heterogeneous, in which case the noise could be greater for posts under thicker parts of the cell (containing more refractile sub-cellular components), and smaller or negligible for posts under very thin parts of the cell. In this case the actual population of decoupled, low-traction force posts/time segments could be much larger than 1% of the data, and the "control" posts analyzed above merely a subset of such posts in optically thin cell regions. However, this effect is ruled out by the observation that the "control" posts were randomly distributed under the cells, in both thick and thin regions (Supplementary Fig. S12*B-D*). Notably, 24 of the 159 control posts/segments were found at the cells' edges, a potential region of high intracellular activity.

Another confounding possibility could be due to apparent post deflections from travelling actin polymerization waves, which have been observed in the basal cortices of many cultured cell types (14, 15). While these are typically observed using confocal or TIRF microscopy, they can also be detected in white-light DIC microscopy (16) in very thin cell processes. Examination of the images in the latter indicate that the refractive contrast from the actin waves is much less than other cellular components such as lipid granules and organelles. Since such components

were already shown in this analysis to contribute negligible optical noise to the post deflections, we can conclude that the effect from actin waves (if present in our cells) would also be negligible.

Assessment of the role of caging effects on micropost MSDs.

The micropost tips used to track cellular fluctuations in this experiment feel an elastic restoring force to return to their resting locations, unlike the free, intracellular tracers used by other researchers e.g. (12). In principle, such a restoring force can "cage" the microposts' trajectories, resulting in the MSDs rolling over at long times. However, based on the following arguments, such effects are not the origin of the unusual forms of the MSDs we observe.

First, at the frequencies and timescales we probed, the magnetically actuated microrheology measurements (Fig. 1*E* and Supplementary Fig. S2) show that the cells are stiffer than the posts. Specifically, from the separate measurements of the posts after removal of the cells via trypsinization (Supplementary Fig. S2) we found that cells' stiffness varied from 1-3 times that of the posts (with an average of 2X) at the lowest frequency probed, 0.1 Hz. From the weak frequency dependence observed, we estimate that the post stiffness would not begin to dominate that of the cytoskeleton until one reaches mHz frequencies i.e., timescales longer than several hundred seconds, and then only for the softest cell responses we observed.

Second, single-post MSDs intermittently show both apparent caging and non-caging behavior, (Fig. 5), resembling free tracer results (12). Specifically, Fig. 5 shows that even for MSDs averaged over 300 s intervals, some trajectories show plateaus starting as early at 10 s lag time, while other MSDs for *the same post* show no plateau out beyond 100 s. As discussed in the main text, this appears to be a consequence of the anomalous statistics and intermittent dynamics of cytoskeletal fluctuations. Notably, for free tracer data, as in Fig. 6 of Ref. (12) the MSDs also show non-reproducible plateaus. Taken together these results suggest that the differences between free tracer MSDs and our posts due to caging effects, while presumably becoming prominent at very long times, are small in the 10-100 sec range.

Finally, RMS deflections of our microposts from their resting locations suggest that our MSDs are not caged at 100 s lag time. In a simple "cage diffusion" model, the RMS deflection of the post from its resting location, σ, is related to the plateau of the caged MSD, having amplitude $4\sigma^2$. While this analysis cannot be made quantitative in the face of post-to-post

heterogeneity, the caging plateau implied by RMS deflections of our micropost ensemble is a factor of several times higher than the apparent plateaus seen in some of our single-post MSDs, again confirming that caging effects to our posts would not become dominant until timescales longer than we consider in this study.

Supplementary Table S1. Summary of data for MSD exponents α_c and α_{sf} for cortically associated and stress-fiber associated microposts, respectively. Data for individual posts are shown for Cells 1-4 in Fig. 4. Standard deviations (SD) and the number of posts of each type are listed for each cell. As discussed in the *SI Appendix Statistics* section, average values are $\bar{\alpha}_c$ = 1.17 ± 0.02 (±SE, N_{cells} = 14) and $\bar{\alpha}_{sf}$ = 1.47 ± 0.02 (±SE, N_{cells} = 13), respectively, and the average standard deviations are $\delta\alpha_c$ = 0.20 ± 0.02 (±SD, N_{cells} = 14) for the cortical posts, and $\delta\alpha_{sf}$ = 0.17 ± 0.04 (±SD, N_{cells} = 13) for the stress fiber-associated posts.

	α_c	SD for α_c	$N_{cortical\ posts}$	α_{sf}	SD for α_{sf}	$N_{stressfiber\ posts}$
Cell 1	1.29	0.20	98	1.45	0.17	26
Cell 2	1.16	0.23	84	1.49	0.12	17
Cell 3	1.11	0.21	41	1.35	0.19	23
Cell 4	1.26	0.17	54	1.46	0.21	24
Cell 5	1.19	0.21	26	1.59	0.14	8
Cell 6	1.05	0.23	20	1.51	0.16	2
Cell 7	1.19	0.19	25	1.50	0.21	12
Cell 8	1.19	0.16	49	N.A.	N.A.	0
Cell 9	1.21	0.18	64	1.54	0.04	2
Cell 10	1.19	0.19	24	1.32	0.14	3
Cell 11	1.10	0.21	97	1.50	0.14	2
Cell 12	1.25	0.22	21	1.52	0.15	12
Cell 13	1.15	0.26	58	1.53	0.25	8
Cell 14	1.16	0.21	42	1.44	0.19	32

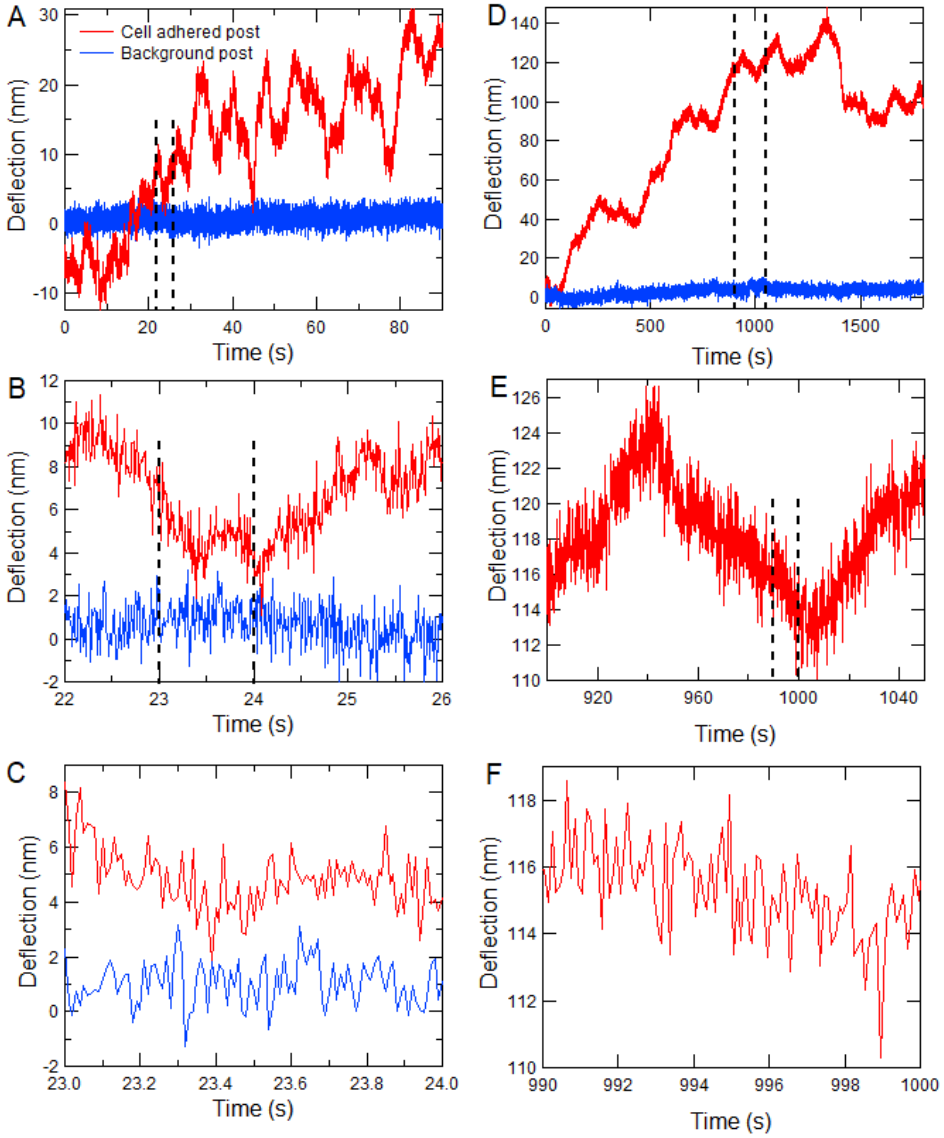

Supplementary Fig. S1. Micropost deflection traces reveal cytoskeletal fluctuations over a wide range of time scales. (*A*) Fluctuations of the x-component of the positions of microposts underneath and outside of a cell, measured at 100 frames/s, reproduced from Fig. 1*C*. (*B*) Expanded view of a portion of the traces shown in *A*. (*C*) Further expansion of a portion of the traces shown in *B* illustrating the high spatial resolution ($\delta x < 2$ nm) of these measurements. (*D*) Fluctuations of micropost positions over an 1,800 s time period, measured at 10 frames/s. (*E*) Expanded view of a portion of the cell-associated micropost's trace in *D*. (*F*) Further expansion of a portion of the trace shown in *E,* illustrating that these longer-duration measurements are sensitive to cytoskeletal fluctuations down to the 0.1 s scale.

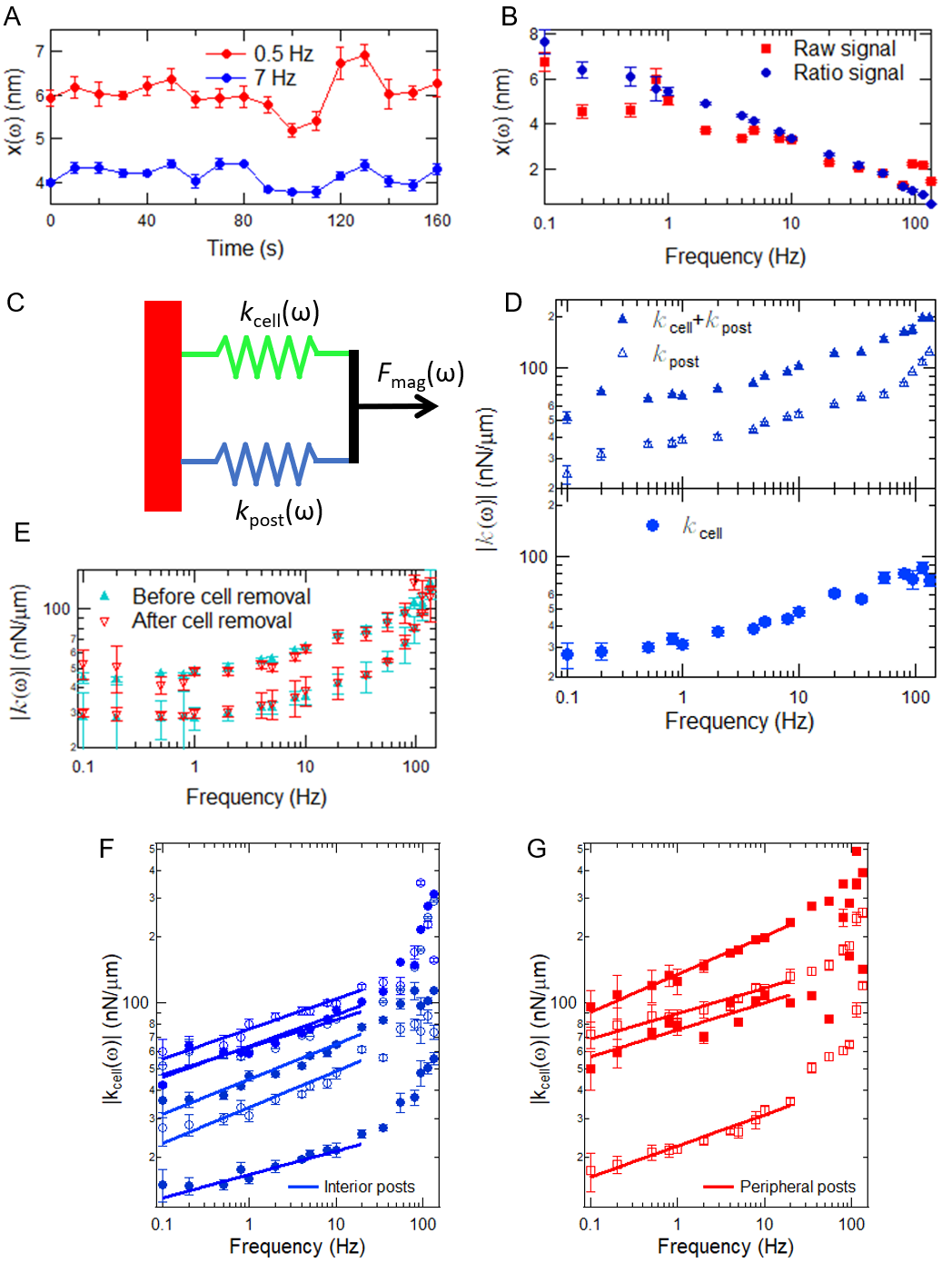

Supplementary Fig. S2. Determination of cellular rheology from AMPAD measurements. (*A*), (*B*) The ratio between responses at two different driving frequencies improves measurements of cytoskeletal rheology. Magnetic microposts' AC response $x(\omega)$ (*A*) to simultaneously applied sinusoidal signals at 0.5 Hz (red) and 7 Hz (blue) showed correlated variation over time. These temporal variations led to significant noise in measurements of the frequency dependence of $x(\omega)$ (*B*, red symbols). An approach that measured the ratio $x(f)/x(f_R)$ (*B*, blue symbols) with f_R = 7 Hz

greatly improved the measurements of the cytoskeletal rheology. (*C*) A cell-coupled magnetic micropost behaves as two viscoelastic units coupled in parallel in response to F_{mag}. (*D*) Upper panel: Frequency dependence of the equivalent stiffness $|k(\omega)| = |F(\omega)/x(\omega)|$ of a post coupled to a cell (solid triangles) and of the same post after removal of the cell trypsin/ETDA (open triangles) measured via magnetic active microrheology. Lower panel: The cellular stiffness $|k_{cell}(\omega)|$ is given by the difference between the above two data sets. (*E*) The frequency dependence of the stiffness of two magnetic microposts that were not coupled to cells, before (solid triangles) and after (open triangles) treatment of the mPAD array with trypsin/ETDA to remove cells from other parts of the array. These measurements showed that the properties of the microposts were not affected by the cell removal process. (*F*) and (*G*) Computed local cellular rheology for interior (cortically associated) and peripheral (stress fiber-associated) microposts showing data points omitted in Fig. 1*E*. Error bars were determined as described in the *SI Appendix Methods* text. All data shown are for individual microposts.

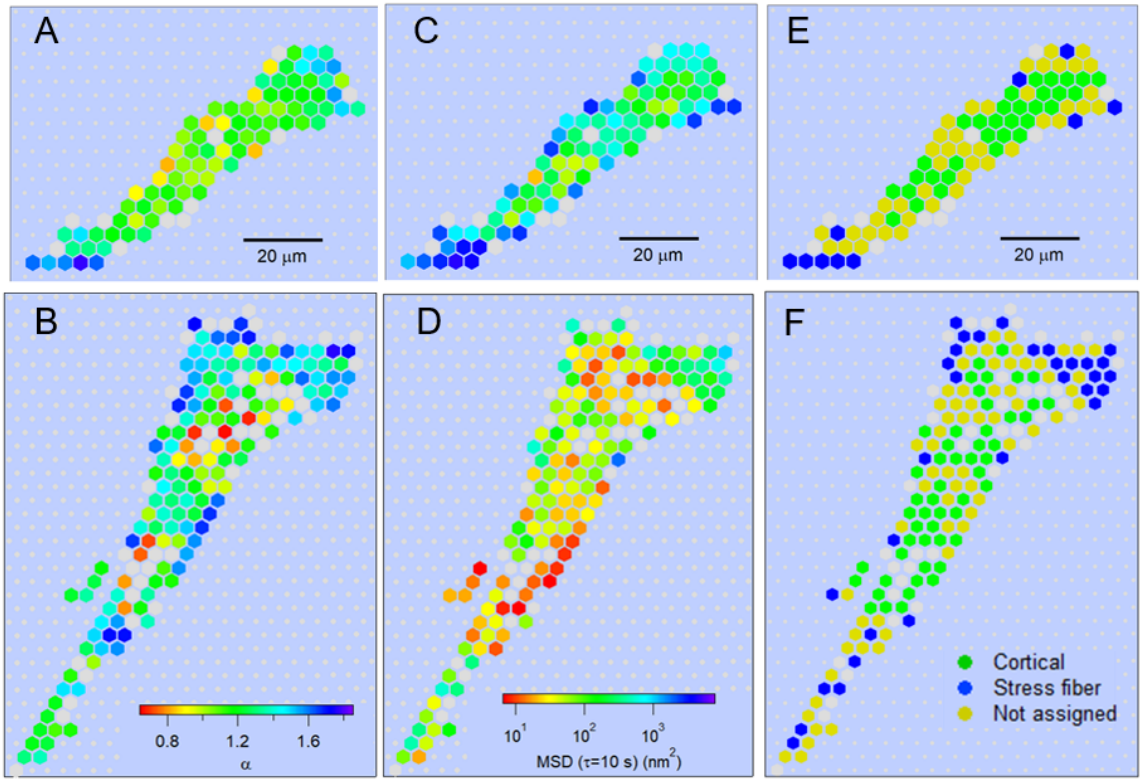

Supplementary Fig. S3. Spatial dependence of the MSD exponent and magnitude, and average AMPAD traction force for two additional cells beyond that shown in Fig. 2. (*A*), (*B*) MSD exponent α for each micropost under a cell, measured in the range 5 s ≤ τ ≤ 10 s. (*C*), (*D*) MSD magnitudes at τ = 10 s. As in Fig. 2, colored hexagons show the MSD exponent or magnitude for posts coupled to cells, grey hexagons indicate posts that were engaged with the cells for only part of the measurement interval, and grey circles indicate background posts. (*E*), (*F*) Classification of microposts according to traction force: maximum traction force < 2 nN (cortically associated posts with low traction force in green); average traction force > 5 nN (stress fiber-associated posts with high traction force in blue); remainder of posts in yellow.

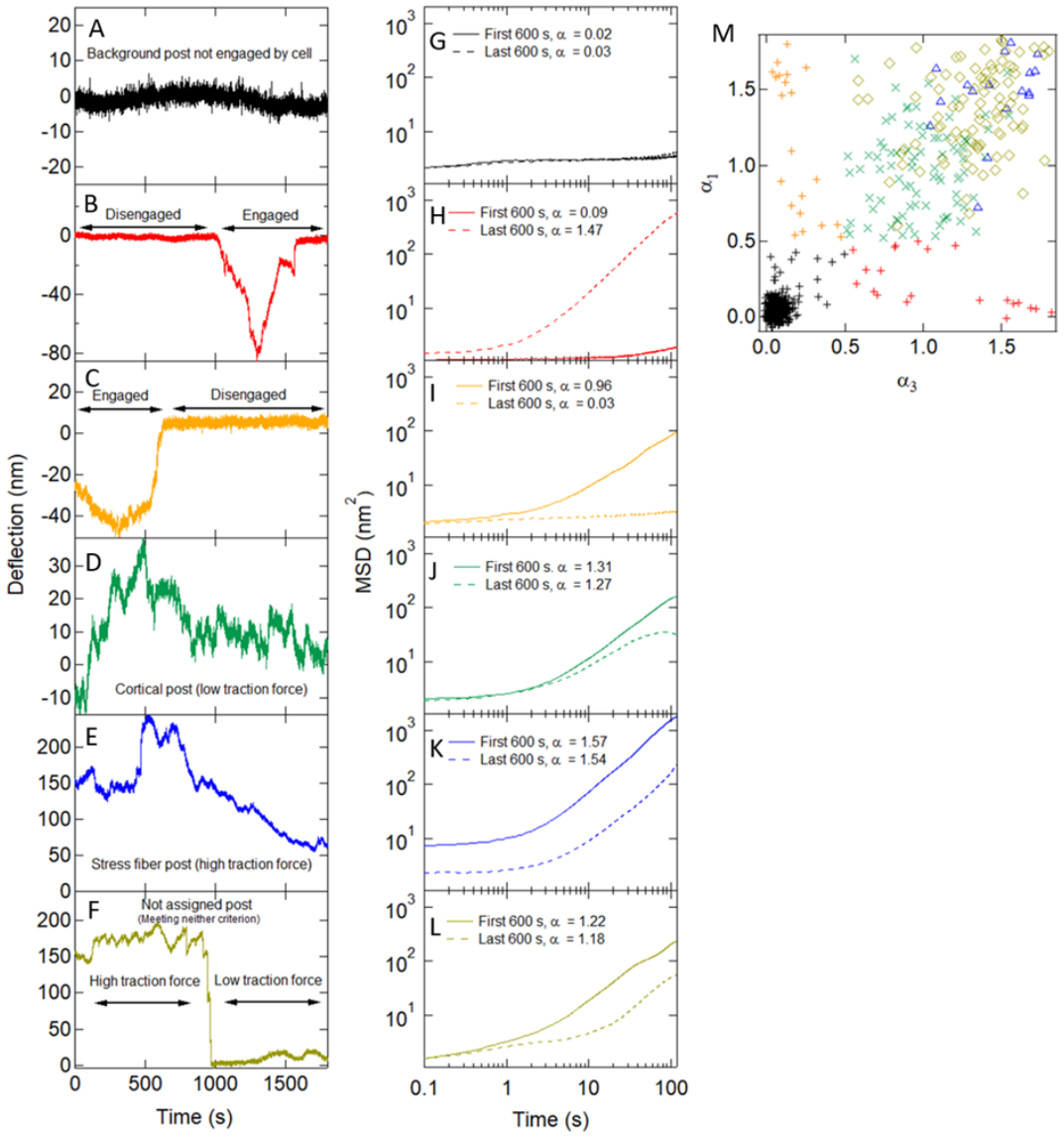

Supplementary Fig. S4. Effects of cell motility on micropost dynamics. (*A-C*) Illustration of the identification of microposts that were engaged with a cell over the full 1,800 s measurement interval via the requirement that the MSD exponents α_1 and α_3 computed over the first and final thirds of the interval, respectively, both be > 0.5. Only the x-component of the microposts' deflections ***r***(t) is shown. (*A*) A "background" micropost that was never in contact with the cell. Such posts are shown as gray circles in Fig. 2 and Supplementary Figs. S3, S5, S6, and S12. (*B*) A micropost engaged with the cell only in the latter part of the measurement interval. (*C*) A micropost initially engaged with the cell, but subsequently released. Microposts such as those shown in *B* and *C* are shown as gray hexagons in Fig. 2 and the Supplementary figures, and were excluded from subsequent analysis. (*D-F*) Illustration of the categorization of cell-engaged

microposts based on their average traction force. (Shown as colored hexagons in Fig. 2 and the Supplementary figures.) (*D*) A cortical micropost with maximum traction force < 2 nN. (*E*) A stress fiber micropost with average traction force > 5 nN. (*F*) A micropost that met neither the cortical nor the stress fiber criteria. Posts such as this were excluded from the subsequent analysis to provide clean separation between the cortical and stress fiber samples, and in particular, to exclude microposts such as the one shown here that made transitions from the high traction force (stress-fiber associated) state to the low traction force (cortically associated) state. (*G*-*L*) MSDs computed over the first and final thirds of the measurement intervals for the traces shown in Panels *A*-*F*. The MSD exponents α_1 and α_3 are given in the figure legend. Error bars on α_1 and α_3 are ± 0.01. (*M*) Scatter plot showing the classification of the microposts under a single cell vs. the MSD exponents α_1 and α_3. The symbol colors correspond to the behaviors illustrated in *A*-*F*, and also in Figs. 2*D*-2*F*, although Fig. 2 shows a different cell. Standard errors in *M* are smaller than the marker size.

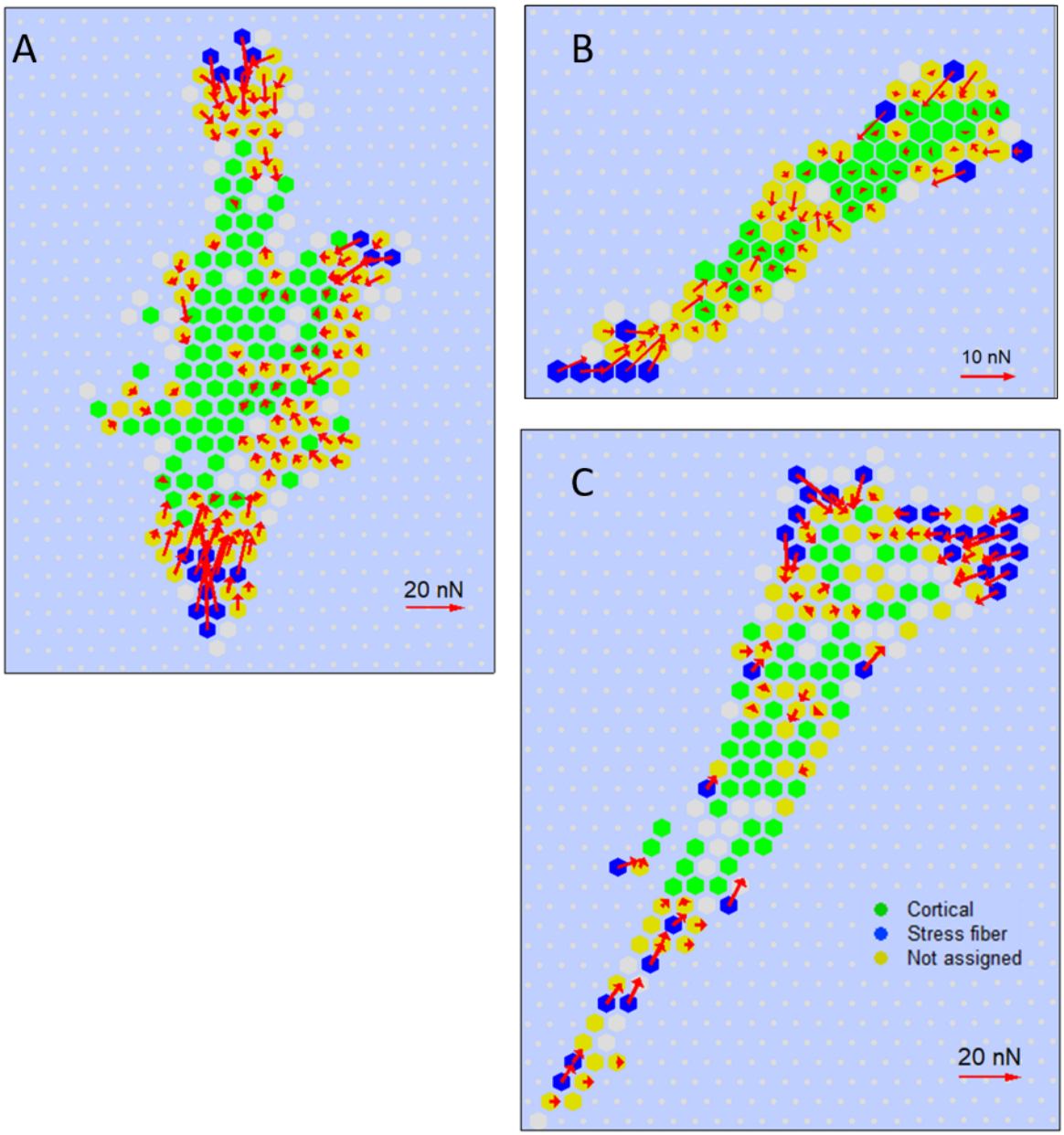

Supplementary Fig. S5. Vector maps of the average traction forces (red arrows) for (*A*) the cell shown in Fig. 2, and (*B*), (*C*) the cells shown in Supplementary Fig. S3. The posts are color coded as in those figures according to our classification based on traction force: maximum traction force < 2 nN (cortical posts with low traction force in green); average traction force > 5 nN (stress fiber posts with high traction force in blue); remainder of posts in yellow.

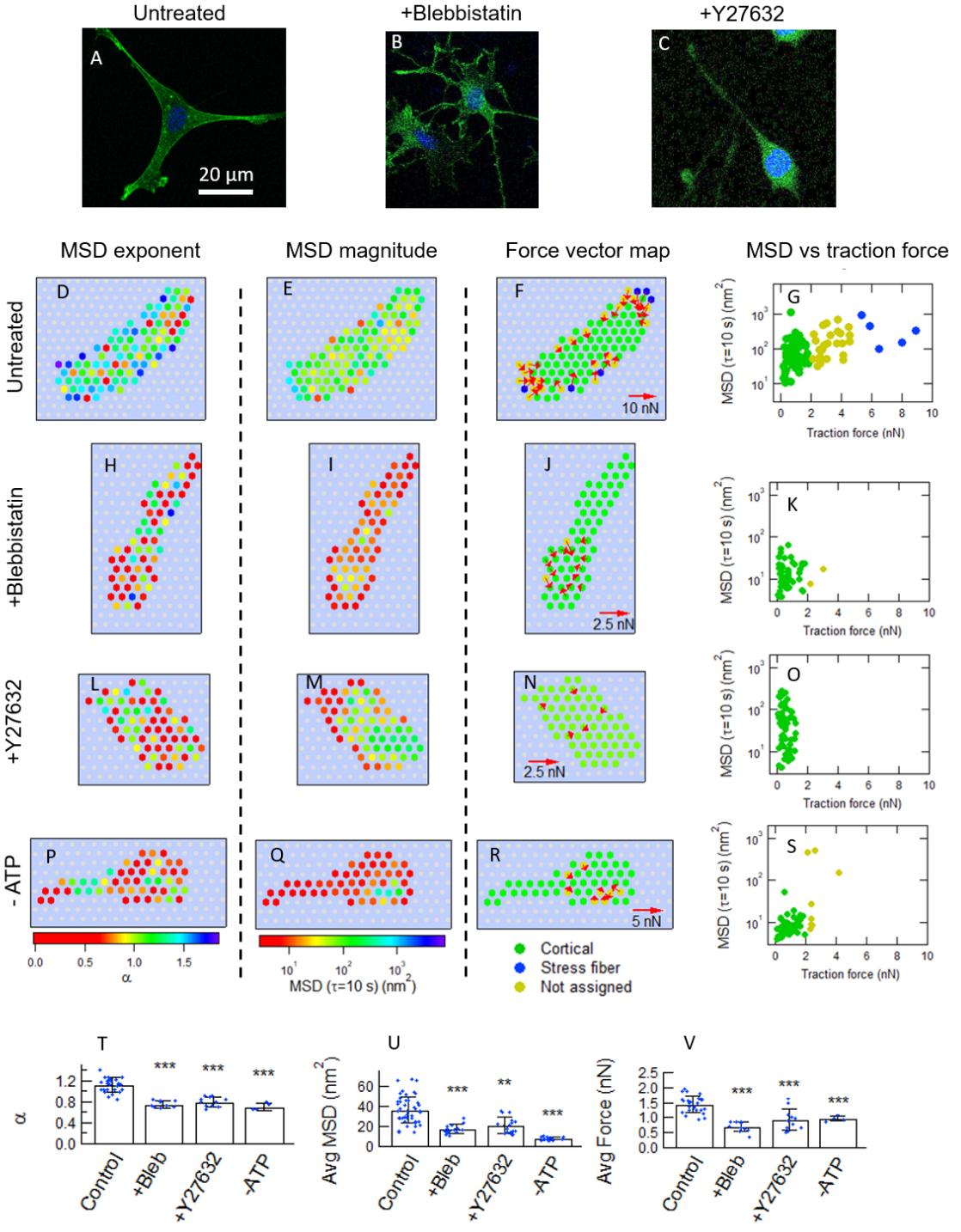

Supplementary Fig. S6. Influence of myosin inhibition on micropost MSDs. (*A*) Untreated, (*B*) Blebbistatin-treated and (*C*) Y27632-treated cells showed morphology changes, with actin distributed more evenly across the cell instead of concentrated more at the cell periphery as was found in untreated cells (see also Fig. 1*B*). Actin was stained with phalloidin (green) and nuclei were stained with Hoechst (blue). (*D*) Distribution of MSD exponent α, (*E*) MSD magnitude at τ

= 10 s, (*F*) vector map of average traction force together with classification of microposts according to traction force as in Fig. 2*D* and Supplementary Fig. S5, and (*G*) corresponding scatter plot of MSD magnitude vs. traction force for an untreated 3T3 fibroblast cell. Corresponding plots are shown for (*H-K*) cells treated with blebbistatin, (*L-O*) Y27632, and (*P-S*) ATP depletion. The maps of the distributions of MSD exponent (*D, H, L, P*), MSD magnitude (*E, I, M, Q*) and MSD magnitude vs. traction force (*G, K, O, S*) follow the same conventions and scales as described in Fig. 2 and Supplementary Fig. S3. The standard errors in *G*, *K*, *O* and *S* are smaller than the symbol sizes. After inhibition of myosin activity, the MSD exponents, MSD magnitudes and traction forces all decreased, and stress fiber posts were not found. Quantification of effects on cortical posts: (*T*) MSD exponent α measured in the range 5 s $\leq \tau \leq$ 10 s , (*U*) MSD magnitude at $\tau = 10$ s (reproduced from Fig. 2*G*) and (*V*) average traction force for untreated control cells (25 cells), and for cells following treatment with blebbistatin (10 cells), Y27632 (11 cells), or ATP depletion (4 cells); significance via unpaired t-test. ** $p < 0.01$; *** $p < 0.001$. Error bars in *T*, *U* and *V* show ±SD. All analysis was done based on videos with 90 s length.

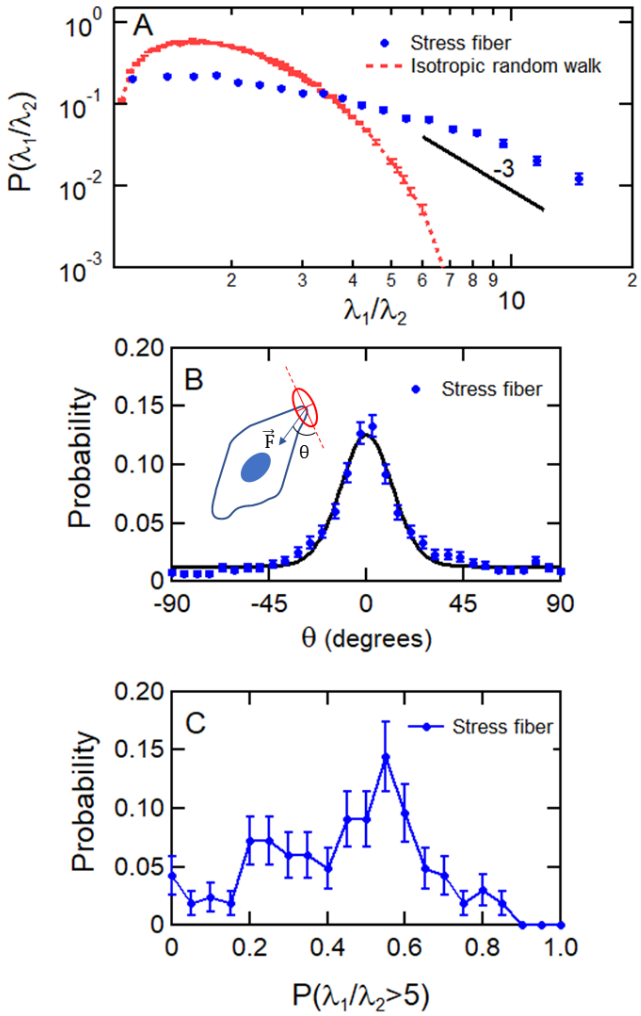

Supplementary Fig. S7. Stress fiber-associated microposts showed strong and persistent anisotropic motion in comparison to cortical posts (Fig. 4) (*A*) Probability distribution of the anisotropy index λ_1/λ_2. Eyeguide highlights a power-law tail for highly anisotropic trajectories. (*B*) Probability distribution of the angle between the major axis of the fitted ellipse's long axis and the direction of the micropost's average traction force $\boldsymbol{F}$ (corresponding to Fig 4*D*). The solid line is a fit with full widths $2\sigma = 24°$. See *SI Appendix Methods* for details. (*C*) Probability distribution of the fraction of a post's fluctuations with $\lambda_1/\lambda_2 > 5$. Measured over 1,800 s in 90 s intervals. (corresponding to Fig 4*E*). Error bars were estimated as $1/\sqrt{N}$ for each bin in the probability distributions.

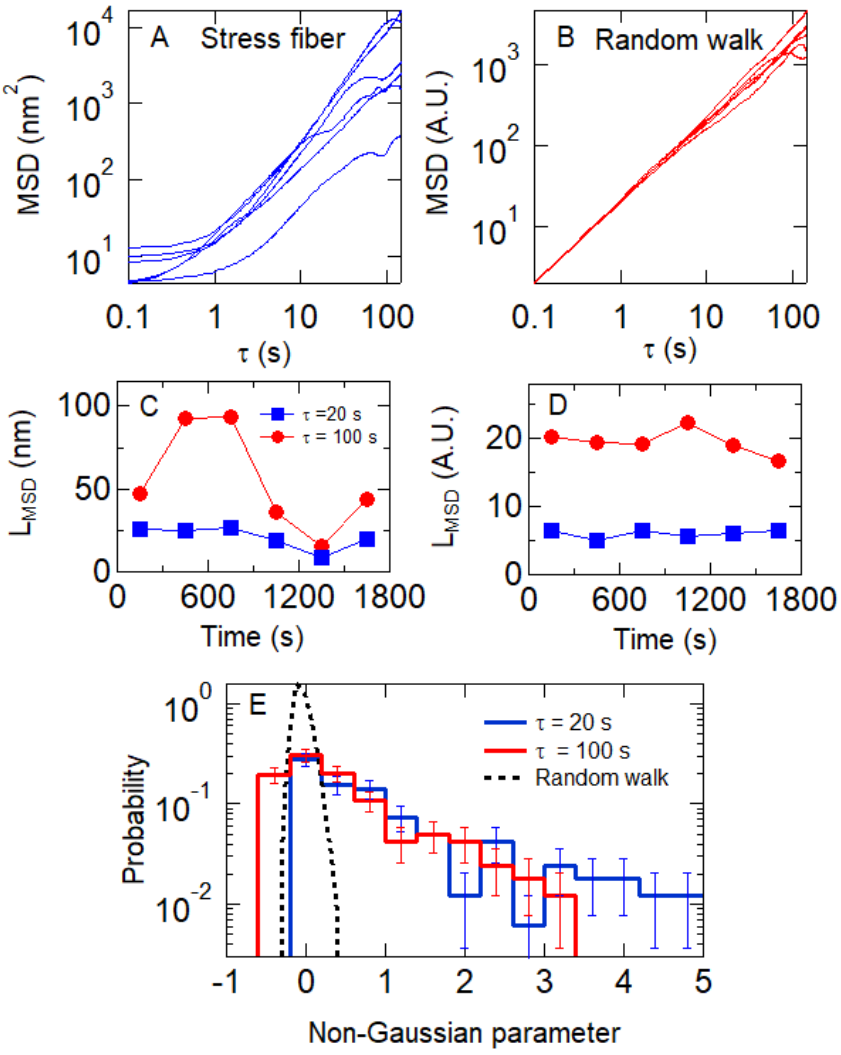

Supplementary Fig. S8. (*A*) Spread of MSDs calculated for a single stress fiber post over each of the six 300 s intervals in the 1,800 s measurement window. (*B*) Simulation showing spread in six MSDs for a Gaussian random walk over the same time interval (Reproduced from Fig. 5*B*). (*C*), (*D*) $L_{MSD} = [MSD(\tau)]^{1/2}$ for τ = 20 s and 100 s for the data shown in *A* and *B,* respectively. (*E*) Distribution of the non-Gaussian parameter, α_2, computed over the full 1,800 s interval for stress fiber posts (N_{cells} = 13). The distribution at τ = 20 s (black dashed line) for an 18,000 step Gaussian random walk is also shown for comparison. Error bars were estimated as $1/\sqrt{N}$ for each bin in the probability distributions.

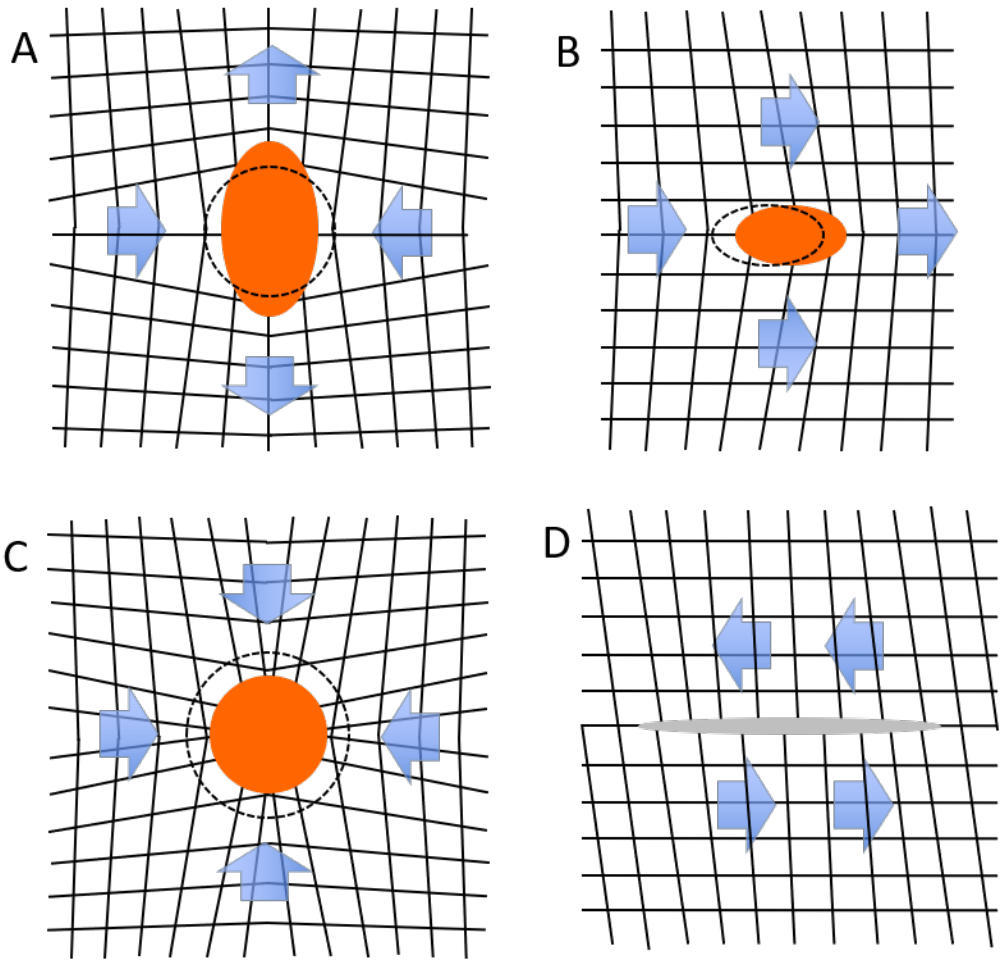

Supplementary Fig. S9. Schematic of the possible symmetries of cortical avalanches. Different strain fields (grid lines) can result from a localized rearrangement in a two-dimensional sheet; the shape change is represented by an initial shape/position (dashed line) and the final configuration (orange solid). (*A*) A local shape change with a quadrupolar symmetry (circle to ellipse) gives rise to a "stresslet" strain field with regions of anti-parallel contraction and expansion (arrows), closely resembling our two-post data. This mode requires no external force, torque or local compression. (*B*) The lateral displacement of small region creates a "stokeslet" strain field consisting of parallel displacements. This mode requires a body force from outside the plane; in the cell case this could consist of abrupt de-adhesion of a small region from the substrate. The lack of our observations of such "parallel" two-post displacements rules out such mechanisms. (*C*) The compression (or expansion) of a small region leads to a "monopole" strain field, and anti-parallel contraction (or expansion). This mode either requires physical compressibility of the network, or out of plane deformation. This mode does not naturally account for why expansion and contraction events in our data are equal in number and show identical amplitudes and dynamics, but is consistent with the observed anti-parallel motion. (*D*) In an externally sheared sheet, a "fault line" (gray domain) can locally relax the network, giving rise to a "rotlet"-like strain field. This is a common mode in earthquakes, but produces displacements that are transverse to the line of centers, which we do not observe.

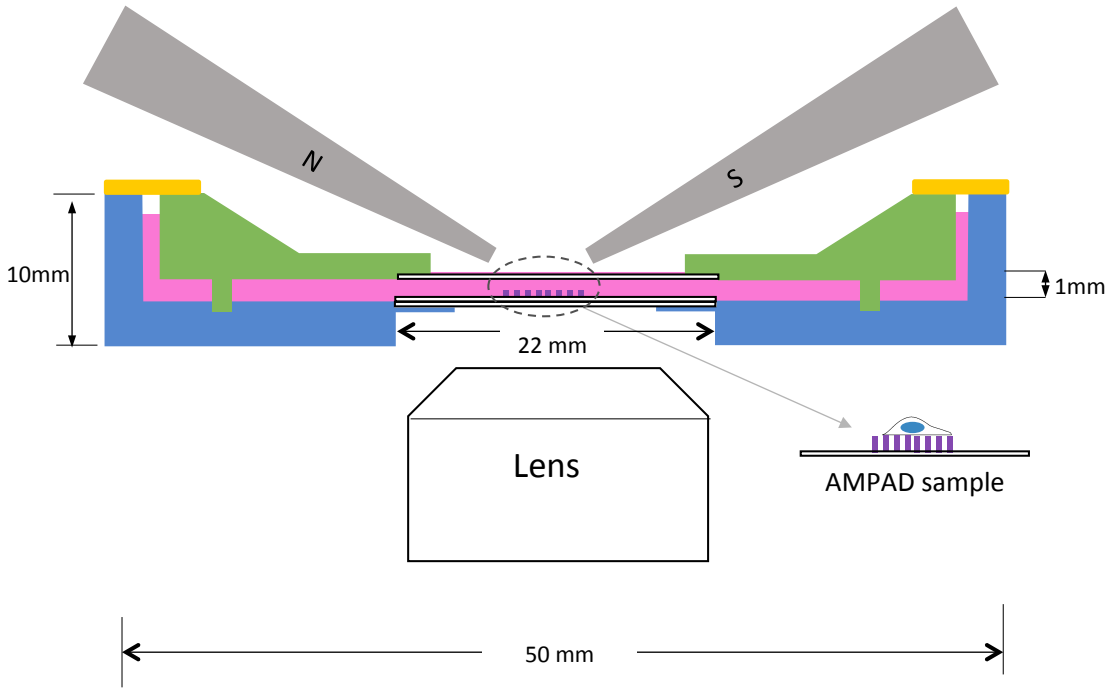

Supplementary Fig. S10. Rheology measurement schematic. A custom 50 mm diameter culture dish was fabricated out of acetal plastic (blue). A standard square coverslip (22 mm width × 0.17 mm thick) (shown in outline) was glued with PDMS into a cutout in the dish to allow optical access. An AMPAD substrate with adhered cells and mounted on a similar coverslip was fit into the cutout on top of the first coverslip. An acetal lid (green) allowed the magnetic tweezer tips (gray) to be brought within 1 mm of the cells without contacting the culture media (pink). The lid had a coverslip glued into it to allow illumination, and the culture media completely filled the volume between the dish and the lid. The lid had four integrated, 2 mm diameter posts in a square pattern that fit into corresponding indentions in the dish to prevent motion of the lid. A PDMS ring (orange) was used to cover the open area between the edge of the lid and the dish to reduce media evaporation.

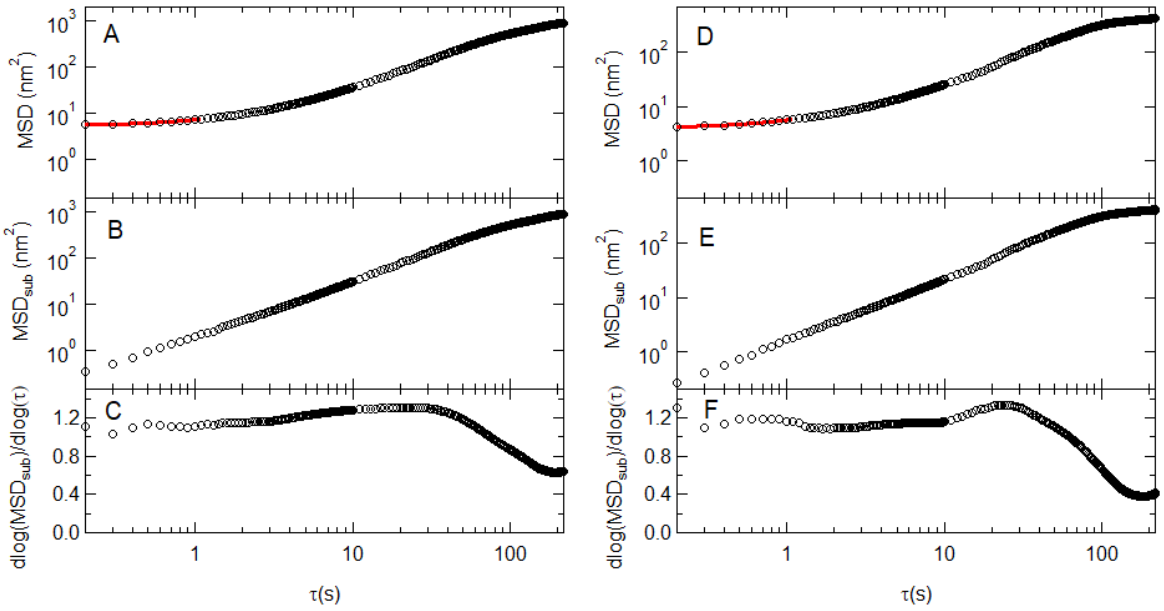

Supplementary Fig. S11. Subtracted MSD and its logarithmic time derivative, illustrating the determination of the MSD exponent α for two microposts. (*A*), (*D*) Raw MSD traces showing fits (red lines) to determine the noise floor as described in the Methods. (*B*), (*E*) MSD traces MSD_{Sub} after subtracting the noise floor from the raw MSDs. (*C*), (*F*) Logarithmic time derivatives of MSD_{Sub}. The MSD exponent α and its uncertainty were obtained from the average of the logarithmic time derivative in the range 5 s ≤ τ ≤ 10 s. The MSDs were computed at 0.1 s intervals in τ, but above τ = 10 s, they are only plotted every 1 s.

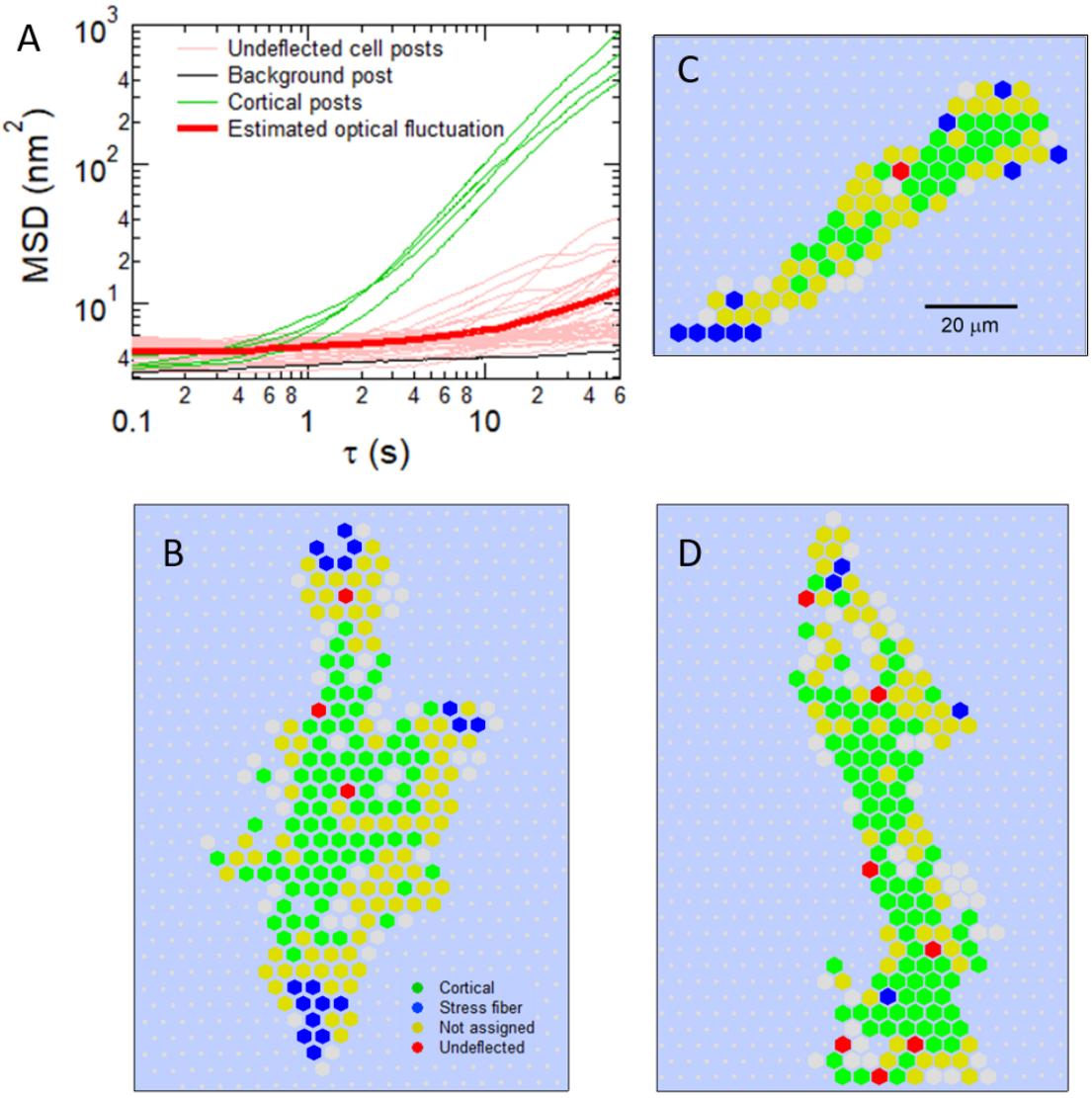

Supplementary Fig. S12. Assessment of impact of fluctuations in cellular optical density on microposts' trajectories and MSDs based on cell-coupled microposts that exhibited 300 s time segments with very small maximum deflections (Δx, Δy < 15 nm) from the posts' resting positions, and correspondingly small maximum traction forces (< 0.24 nN). (*A*) Pink traces: MSDs for 53 such 300 s segments. Red trace: MSD averaged over all 159 such segments in our sample. Black trace: MSD of representative background micropost not coupled to a cell. Green traces: MSDs for representative cortical microposts computed over 300 s intervals. By minimizing effects due to micropost displacement on the MSDs, this measurement sets an upper bound on the contribution of optical density fluctuations to < 10% of the MSD signal for lag times τ > 10 s. (*B-D)* Examples of locations of microposts (red hexagons) included in this measurement, illustrating their distribution throughout the cells.

References

1. Tan JL*, et al.* (2003) Cells lying on a bed of microneedles: an approach to isolate mechanical force. *Proc. Natl. Acad. Sci. U. S. A.* 100(4):1484-1489.
2. Fu JP*, et al.* (2010) Mechanical regulation of cell function with geometrically modulated elastomeric substrates. *Nat. Methods* 7(9):733-736.
3. Tanase M*, et al.* (2001) Magnetic alignment of fluorescent nanowires. *Nano Lett.* 1(3):155-158.
4. Hultgren A, Tanase M, Chen CS, & Reich DH (2004) High-yield cell separations using magnetic nanowires. *IEEE Transactions on Magnetics* 40(4):2988-2990.
5. Hultgren A*, et al.* (2005) Optimization of yield in magnetic cell separations using nickel nanowires of different lengths. *Biotechnol. Prog.* 21(2):509-515.
6. Sniadecki NJ*, et al.* (2007) Magnetic microposts as an approach to apply forces to living cells. *Proc. Nat. Acad. Sci.* 104(37):14553-14558.
7. Sniadecki NJ, Lamb CM, Liu Y, Chen CS, & Reich DH (2008) Magnetic microposts for mechanical stimulation of biological cells: Fabrication, characterization, and analysis. *Rev. Sci. Instrum.* 79(4):044302.
8. Lin YC, Kramer CM, Chen CS, & Reich DH (2012) Probing cellular traction forces with magnetic nanowires and microfabricated force sensor arrays. *Nanotechnology* 23:075101.
9. Massiera G, Van Citters KM, Biancaniello PL, & Crocker JC (2007) Mechanics of single cells: Rheology, time dependence, and fluctuations. *Biophys. J.* 93(10):3703-3713.
10. Crocker JC & Grier DG (1996) Methods of digital video microscopy for colloidal studies. *J. Colloid Interface Sci.* 179(1):298-310.
11. Dixon PK & Wu L (1989) Broad-band digital lock-in amplifier techniques. *Rev. Sci. Instrum.* 60(10):3329-3336.
12. Guo M*, et al.* (2014) Probing the stochastic, motor-driven properties of the cytoplasm using force spectrum microscopy. *Cell* 158:822-832.
13. Bevington PR (1969) *Data Reduction and Error Analysis for the Physical Sciences* (McGraw-Hill, New York).
14. Gerhardt M*, et al.* (2014) Actin and PIP3 waves in giant cells reveal the inherent length scale of an excited state. *J. Cell Sci.* 127(20):4507-4517.
15. Inagaki N & Katsuno H (2017) Actin waves: Origin of cell polarization and migration? *Trends Cell Biol.* 27(7):515-526.
16. Giannone G*, et al.* (2004) Periodic lamellipodial contractions correlate with rearward actin waves. *Cell* 116(3):431-443.